Supplementary Information

Low absorption losses of strongly coupled surface plasmons in nanoparticle assemblies

Wei-Shun Chang[a], Britain A. Willingham[a], Liane S. Slaughter[a], Bishnu P. Khanal[a],

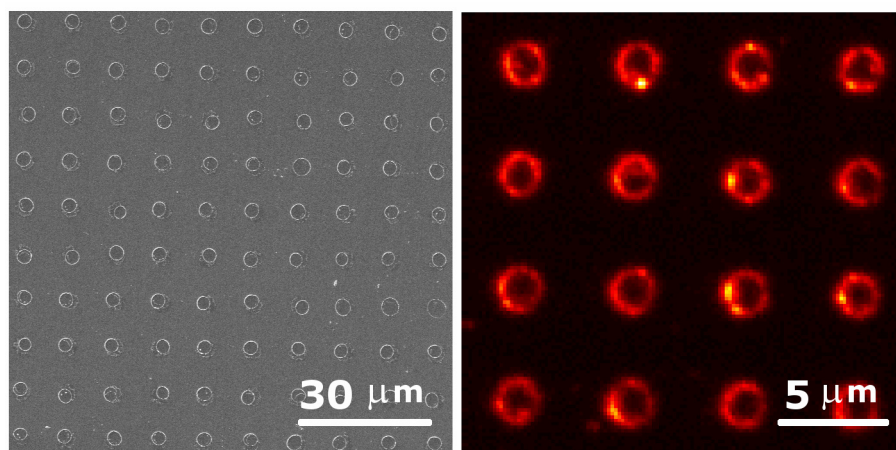**Leonid Vigderman[a], Eugene R. Zubarev[a], and Stephan Link[a,b,1]**

[a]Department of Chemistry, [b]Department of Electrical and Computer Engineering

Laboratory for Nanophotonics, Rice University, Houston, TX, 77005

[1]To whom correspondence should be addressed. E-mail: slink@rice.edu

CONTENTS: **Page**

Fig. S1 SEM (left) and scattering (right) images of an array of NP rings. The optical image was taken for a smaller area in order to clearly show the structure of the rings given the lower resolution. Arrays of NP rings were fabricated by first patterning arrays of circular hydrophilic areas with a hydrophobic background through the use of microcontact printing (1). A silicon wafer master was coated with photoresist and patterned on a Heidelberg DWL66 Laser Writer. A polydimethylsiloxane (PDMS) stamp was then cast from this master by pouring over it a mixture (10:1 by mass) of PDMS pre-polymer (Sylgard 184, Dow Corning) and curing agent, degassing the mixture, and heating at 70 °C for 1 hour. Hydrophilic regions were then patterned onto a gold-coated glass slide by stamping of a 2 mM solution of 16-mercaptohexadecanoic acid in ethanol, followed by dipping into a 2 mM solution of hexadecanethiol in ethanol to form the hydrophobic background, and then rinsing with ethanol. The substrate was cooled to 5-10 °C and briefly exposed to moist air. The condensation of water occurred almost exclusively on the hydrophilic sites and created a periodic array of near monodisperse water droplets. Finally, a methylene chloride solution of polystyrene-functionalized nanoparticles was cast onto the substrate leading to the formation of a periodic array of NP rings after drying.
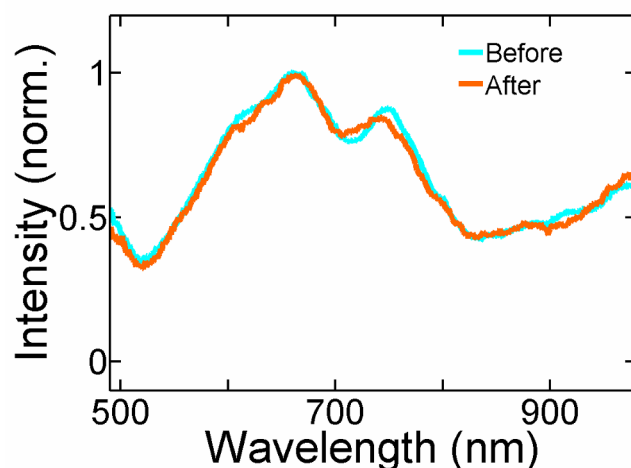
Fig. S2 Scattering spectra of the ring segment before (cyan) and after (orange) photothermal imaging to show that the heating and probe laser beams did not melt the NPs and alter the NP ring structure.
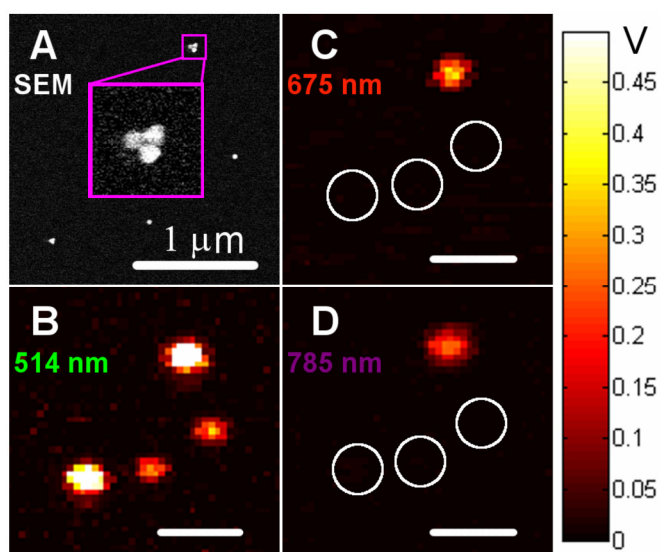

Figure S3. Wavelength dependent absorption of single gold NPs and a NP trimer. Because of the high sensitivity of photothermal heterodyne imaging, excitation of the long wavelength tail of the single NP resonance at 785 and 675 nm can be ruled out. Correlated SEM (A) and photothermal images recorded with 514 (B), 675 (C), and 785 (D) nm excitation were collected for single NPs and a trimer. At 514 nm both the trimer and the single NPs were visible, while at 675 nm and 785 nm only the trimer was observed. The white circles in (C) and (D) indicate the position of the single NPs. If the absorption intensities at 675 and 785 nm scaled linearly with number of NPs, then based on the signal to noise ratio and background levels in (C) and (D), the individual NPs would be visible as well. This is furthermore consistent with the observation that the scattering intensity of 40 nm NPs at 785 and 675 nm is zero (Fig. 1B) and that calculations predict very similar spectral profiles for absorption and scattering of NPs in this size range. Therefore, these results indicate that the absorption images of the ring for excitation at 785 and 675 nm are due to coupled SPs.

Comparison of photothermal intensities of isolated NPs and NP ring at 514 nm

The photothermal intensities of single isolated NPs and NPs in the ring were compared to show that at 514 nm the absorption intensity of the ring approximately scales with the number of NPs per area. The same 40 nm NPs that were used to assemble the NP ring were drop-casted on a glass slide followed by spin-casting a polyvinyl alcohol (PVA) film to ensure a homogenous sounding medium. Single NPs were identified by SEM. The heating and probe wavelengths for the photothermal measurements were 514 and 633 nm, respectively. For single NPs, the excitation power was 500 μW. The excitation power for the NP ring was 50 μW to avoid saturating the signal. The probe power was 800 μW for both measurements. Fig. S4A shows a photothermal image of 40 nm NPs with 514 nm excitation. The intensities were integrated for 390 x 390 nm^2 areas indicated by the white boxes, which was based on the optical resolution of the photothermal images. Fig. S4B shows a photothermal image of the NP ring with 514 nm excitation. The intensities were integrated for the same areas of 390 x 390 nm^2 as shown again by the white boxes. To compare the intensity per particle of single isolated NPs and individual NPs in the ring assembly, the intensities of the different ring segments were normalized by the number of NPs contained in each of the white boxes and then scaled to an excitation power of 500 μW. The number of NPs was obtained by overlaying the photothermal and SEM images.

Fig. S5 displays the power dependence of the photothermal intensity for 40 nm NPs with 514 nm excitation. The red line is a linear regression. The photothermal intensity scales linearly with the excitation power which is consistent with previous results(2) and therefore justifies the linear scaling factor used for the intensity comparison.
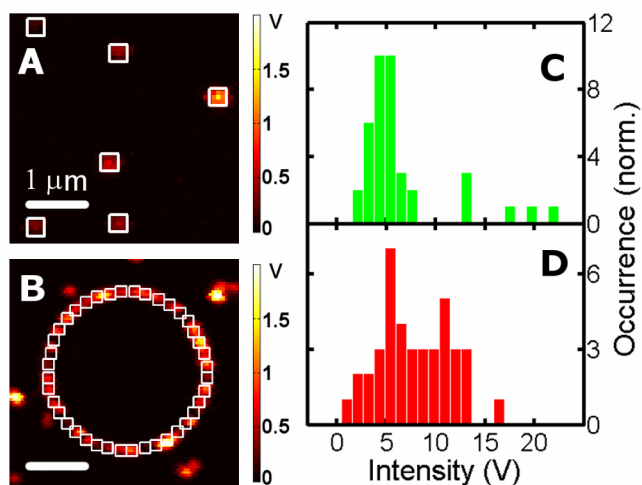
Fig. S4 Photothermal intensity of NPs with 514 nm excitation. (A), (B) photothermal images (6.7 x 6.7 μm²) of 40 nm NPs and the NP ring for 514 nm excitation, respectively. (C) histogram of photothermal intensity of single isolated 40 nm NPs with excitation power of 500 μW. (D) histogram of photothermal intensity of 40 nm NPs in the ring with excitation power of 50 μW. The intensities were normalized by the number of NPs per excitation volume and scaled to the excitation power of 500 μW.
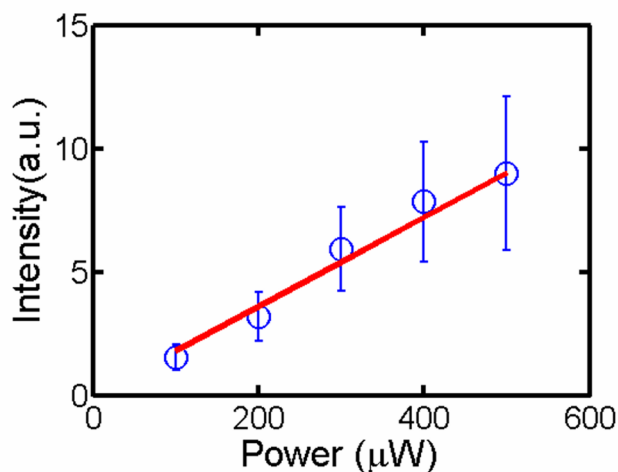

Fig. S5 Power dependence of the photothermal intensity for 40 nm NPs with 514 nm excitation. The error bar represents the standard deviation of the intensity from several NPs. The red line is a linear regression.

Figs S4C and S4D show the photothermal intensity histograms of single isolated NPs and single NPs in the ring assembly, respectively. The intensity distributions are comparable. The distribution of isolated NPs is slightly narrower than that of the NPs in the ring. However, several isolated NPs show higher intensities due to size inhomogeneity because larger triangular

NPs were also present as verified by correlated SEM imaging. The intensity histogram of single NPs in the ring assembly is broader, but the maximum intensity is not as large as those of the larger triangular NPs. Because the intensity of the NPs in the ring was normalized by the number of NPs for each integration area, the contribution from larger triangular NPs is averaged with the intensities of spherical NPs. This effect appears to lead to an apparent higher intensity per NP for some areas and hence results in the broader intensity histogram observed for the NPs in the ring assembly. Therefore, the intensities of single isolated NPs and NPs in the ring are comparable for 514 nm excitation.

Dark-field scattering is significantly less sensitive, making the same comparison to individual 40 nm NPs more difficult. However, based on the similar intensity distributions for absorption and scattering, as shown in Figs. 1E and 1H, the same conclusion should also apply for scattering.
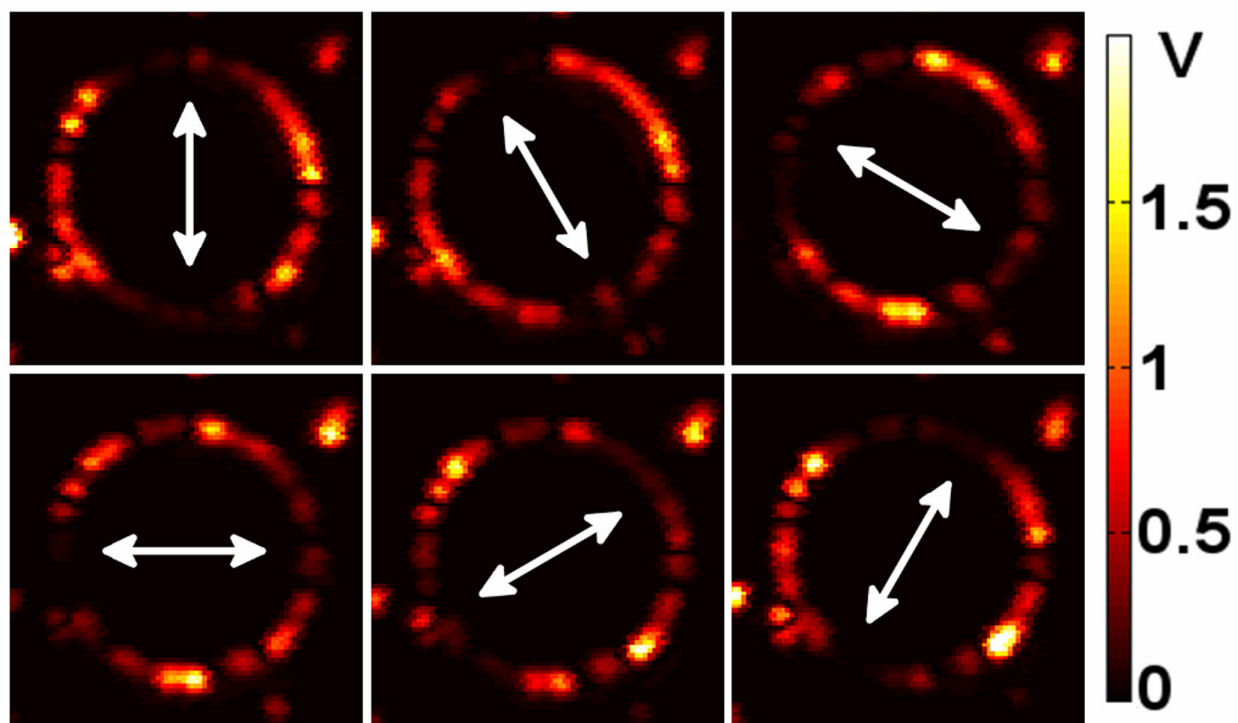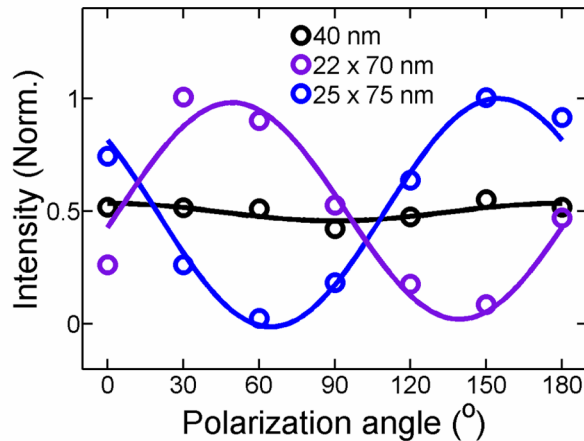

Fig. S6 Polarized photothermal images of the NP ring for 785 nm excitation. The arrows represent the direction of excitation polarization.
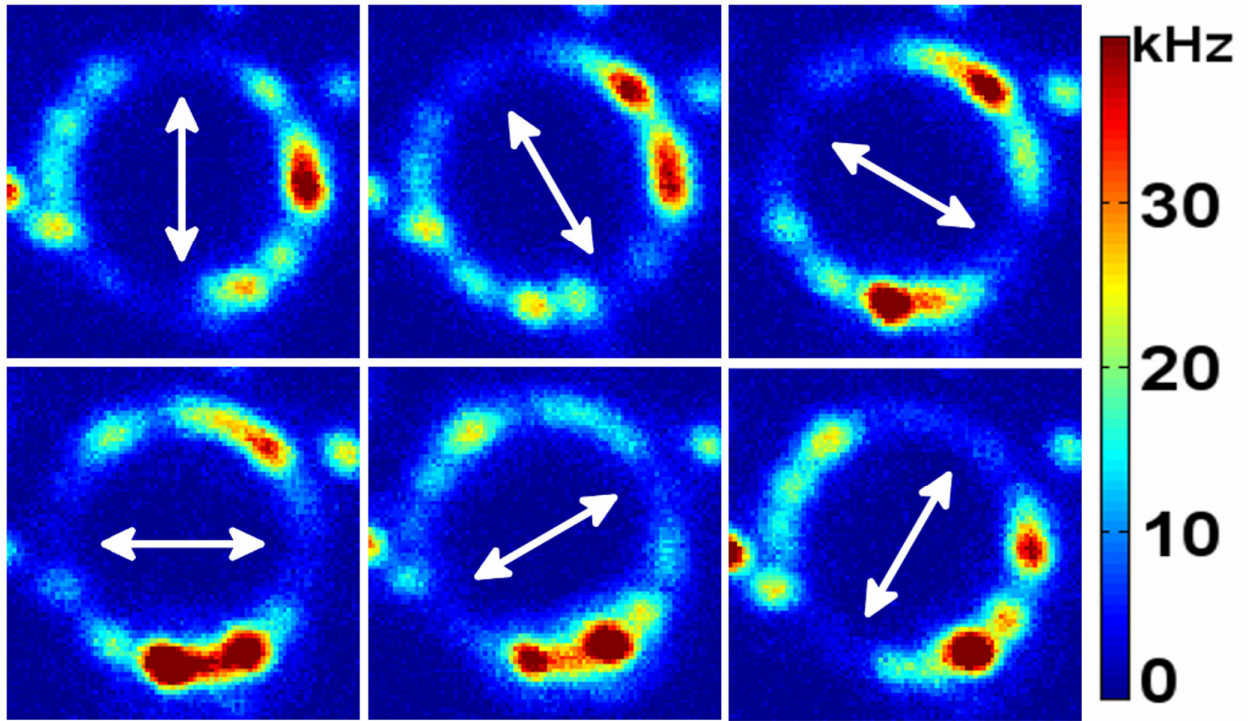
Fig. S7 Polarized scattering images of the NP ring recorded for a spectral window of 800 ± 20 nm. The arrows represent the direction of detection polarization.

Fig. S8 Polarization dependence of the photothermal intensity for a single spherical NP (40 nm) with 514 nm excitation (black circle), a single nanorod (22 x 70 nm) with 785 nm excitation (purple), and a single nanorod (25 x 75 nm) with 675 nm excitation (blue). The lines show fits of the data points to $I(\theta) = N(1 + M \cos 2(\theta - \phi))$. The recovered modulation depth M was 0.08 for the almost spherical NP consistent with an isotropic SP oscillation. In contrast, the modulation depths M for the 22 x 70 nm and 25 x 75 nm nanorods were 0.96 and 1.02, respectively. This confirms our ability to measure by polarization sensitive photothermal imaging a maximum modulation depth of unity as expected for the longitudinal dipole mode of a nanorod.
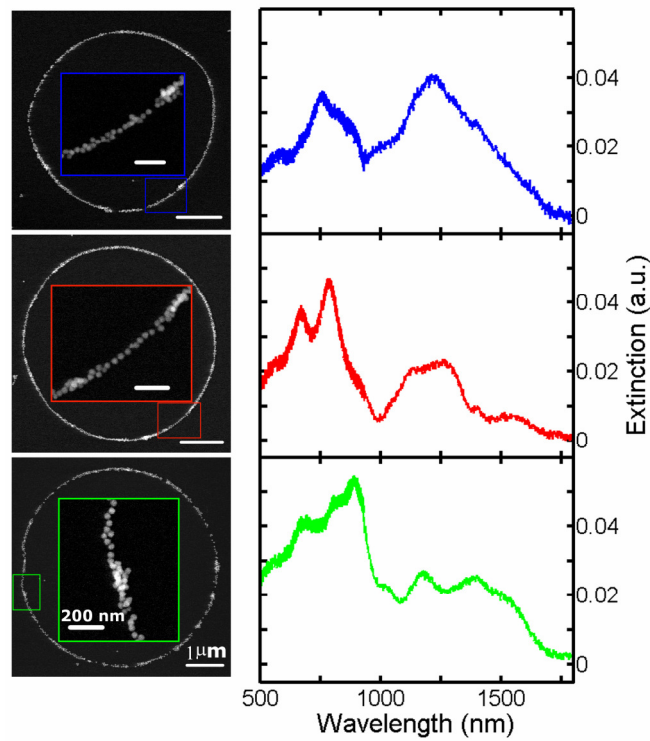
Fig S9 Unpolarized extinction spectra of local segments for different NP rings. The diameters of the rings were 4.1(top), 4.6 (middle) and 5.6 (bottom) μm. The fact that the maxima of the different SP modes did not change significantly for different ring diameters confirms that the observed optical response originated from local NP segments and were not due to modes delocalized over the entire ring. In addition, independent of the ring and the local segment all spectra show SP resonances beyond 1000 nm that were assigned to SP coupling between touching NPs.
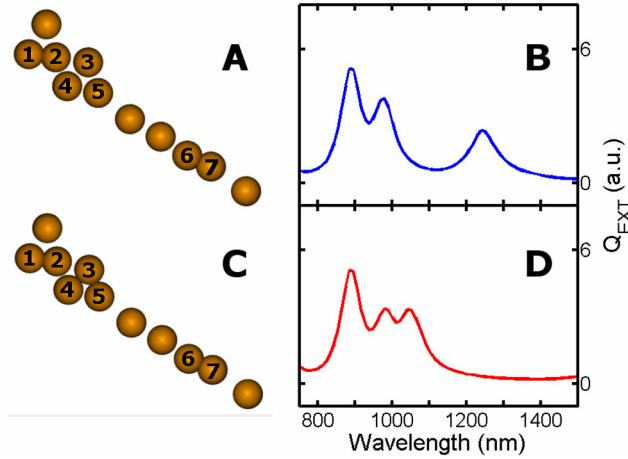
Fig. S10 FEM calculations of a local ring segment considering conductive coupling between neighboring NPs. The NP geometry is given in (A) and (C) and the corresponding extinction spectra are shown in (B) and (D). The excitation polarization was parallel to the long axis of the NP arragment. In (A), two groups of NPs were touching (NPs #1, 2, and NPs #6, 7). In (C), three groups of NPs were touching (NPs #1, 2, NPs #3, 4, 5, and NPs #6, 7).

Calculation of σ$_{SCA}$ for the NP ring

The scattering cross section σ$_{SCA}$ for a ring of NPs was calculated by obtaining the ratio of the scattering intensities from the NP ring (I$_{SCA,Ring}$) and a single NP (I$_{SCA,NP}$) and then multiplying this ratio by the theoretical σ$_{SCA,NP}$ of a single NP, as given in eq. S1.

$$\sigma_{SCA,ring} = \sigma_{SCA,NP} \times \frac{I_{SCA,ring}}{I_{SCA,NP}} \tag{S1}$$

σ$_{SCA,NP}$ was calculated by solving Maxwell's equations for a known size of the NP and the dielectric constants of the metal and surrounding medium. To obtain efficient scattering intensities for single NPs at 800, 700, and 550 nm, we selected NPs with average sizes of 22 x 70 nm, 33 x 63 nm, and 96 nm which were first characterized by TEM (Fig. S11A-C). The size distributions of each sample were 22 ± 4 x 70 ± 11 nm, 33 ± 5 x 63 ± 12 nm and 96 ± 7 nm (Fig. 11D), respectively. The error corresponds to the standard deviation of the NP size. The scattering

spectra of the NPs were calculated by FEM using the software COMSOL Multiphysics assuming the average size for each NP sample and a homogenous embedding medium with a refractive index of 1.5 (Fig. S12A).
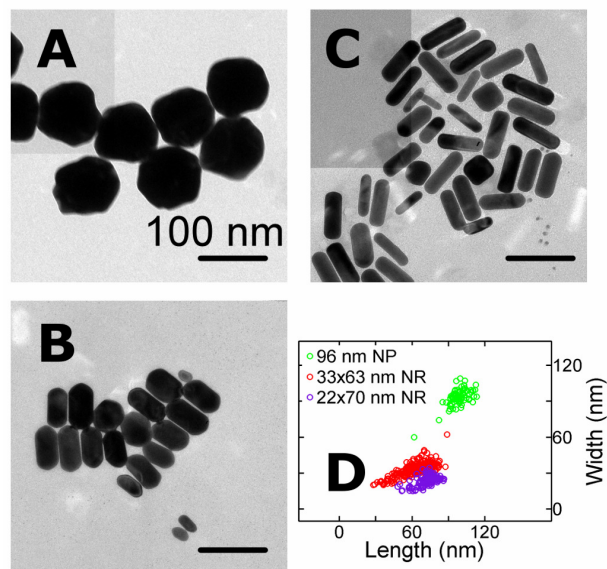

Fig. S11 TEM images of 96 nm (A), 33 x 63 nm (B), and 22 x 70 nm (C) NPs. The scale bars represent 100 nm for all images. (D) size distribution of the three NP samples.
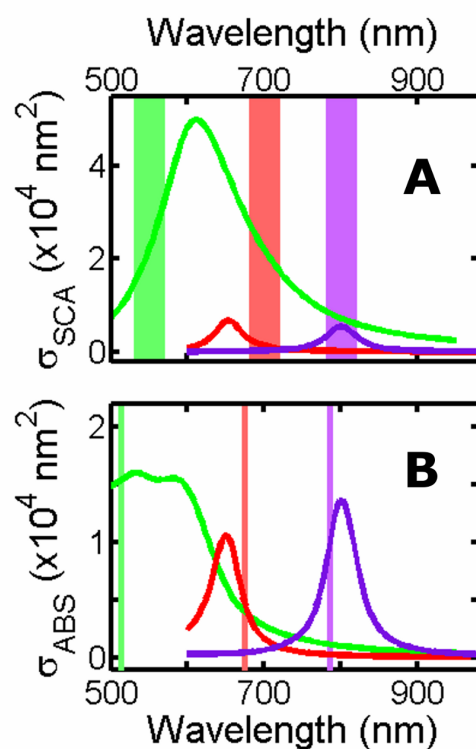
Fig. S12 Calculated scattering and absorption cross sections of NPs. Calculated scattering (A) and absorption (B) spectra of 96 nm (green), 33 x 63 nm (red) and 22 x 70 nm (purple) NPs using the software COMSOL Multiphysics. The refractive index of the medium was chosen to be 1.5. The green, red, and purple bars in (A) mark the detection wavelengths of 550 ± 20, 700 ± 20, and 800 ± 20 nm, respectively. The green, red, and purple lines in (B) mark the excitation wavelengths of 514, 675, and 785 nm, respectively.

In order to measure the scattering intensities of the single NPs, we drop-cast the NP solution on a pre-cleaned glass slide, which was followed by spin-casting a thin layer of PVA film to ensure a homogeneous surrounding medium with a refractive index of 1.5. The scattering spectra of the single NPs were measured by dark-field microscopy and fit to a Lorentzian function as expected for single NPs (Fig. S13). Only NPs with a peak wavelength within ± 10 nm of the predicted value based on the mean size of the experimental distribution (Fig. S12A) were selected. About 20 NPs of each sample were chosen following this procedure. The scattering intensities of the three NP samples with average sizes of 22 x 70, 33 x 63, and 96 nm were then measured by dark-field microscopy using bandpass filters of 800 ± 20, 700 ± 20, and 550 ± 20 nm. Fig. S14A shows a scattering image of 96 nm NPs recorded with a bandpass filter

of 550 ± 20 nm. The intensities of the selected NPs were integrated over a 850 x 850 nm^2 area, which was the resolution for the scattering image and is represented by the white boxes in Fig. S14A. The 96 nm NPs were chosen because the scattering intensity of individual 40 nm NPs was too low to yield reliable results. The same procedure was performed for the 22 x70 and 33 x 63 nm NPs using bandpass filters of 800 ± 20 and 700 ± 20 nm, respectively. In this way, we determined the measured scattering intensities ($I_{SCA,NP}$) for each sample.
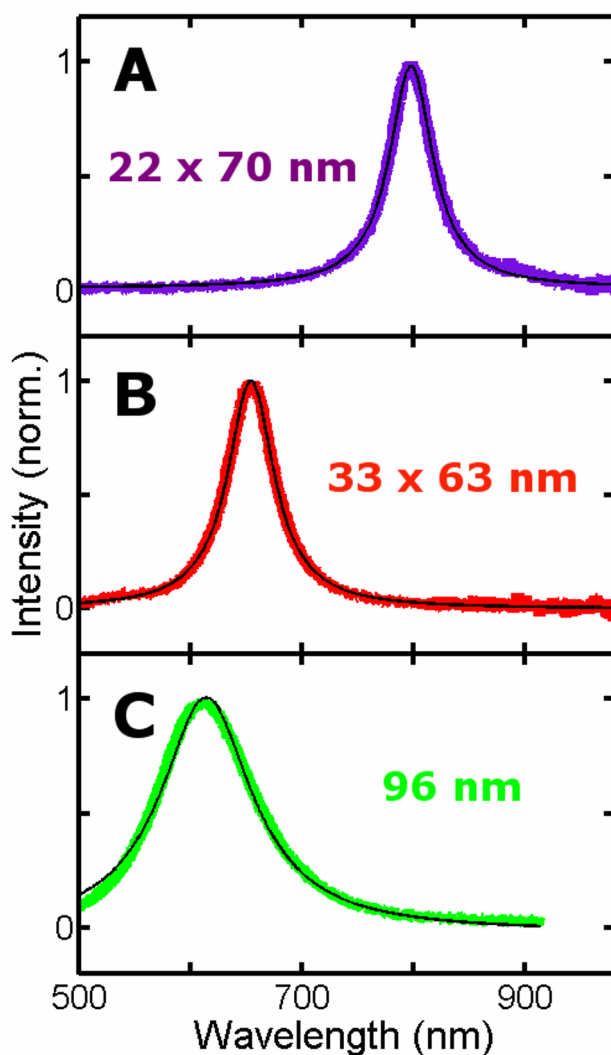
Fig. S13 Scattering spectra of single NPs. Representative spectra are shown for NPs taken from the samples with average sizes of 22 x 70 (A), 33 x 63 (B), and 96 nm (C). The black lines are fits to a Lorentzian function, which is the expected line shape for single NPs.
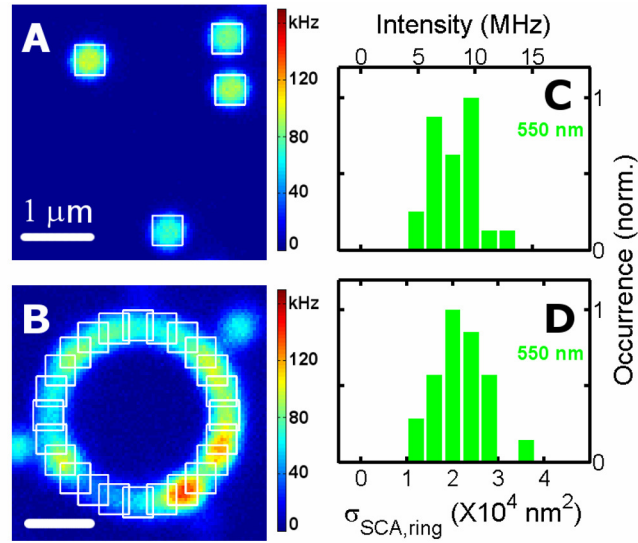
Fig. S14 Calculation of σ_{SCA} for a NP ring. (A), (B) Scattering images (6.7 x 6.7 μm^2) of 96 nm NPs and the NP ring recorded with a 550 ± 20 nm bandpass filter, respectively. The white boxes (850 x 850 nm^2 each) represent the integration areas used for calculating the scattering intensity. (C) Histogram of integrated scattering intensities for the NP ring, where the integrated area corresponds to the size of the white boxes in (B). (D) Histogram of $\sigma_{SCA,ring}$ for the NP ring calculated using eq. S1.

The calculated $\sigma_{SCA,NP}$ of the 22 x 70, 33 x 63 and 96 nm NPs were obtained by integrating the simulated scattering spectra for the spectral windows of 800 ± 20, 700 ± 20, and 550 ± 20 nm and then normalized by the band width of the filter (40 nm), respectively. In Table S1 the scattering intensities and $\sigma_{SCA,NP}$ for each NP sample are given.

Table S1: Summary of the scattering intensity and σ_{SCA} for individual NPs (error is the standard deviation)

Sample (detection window)	$I_{SCA,NP}$ (MHz)	$\sigma_{SCA,NP}$ (nm^2)
96 nm (550 ± 20 nm)	7.4 ± 0.7	2.1 x 10^4
33 x 63 nm (700 ± 20 nm)	1.7 ± 0.9	1.5 x 10^3
22 x 70 nm (800 ± 20 nm)	2.6 ± 1.5	4.6 x 10^3

The scattering intensities of the NP ring were acquired with bandpass filters of 800 ± 20, 700 ± 20, and 550 ± 20 nm. Note that the scattering images of the NPs and the NP ring were measured side-by-side for each wavelength to ensure the same experimental conditions. The

intensities of the ring segments ($I_{SCA,ring}$) were also acquired by integrating areas of 850 x 850 nm^2 along the ring to compare to the single NPs. Fig. S14B shows the scattering image of the NP ring taken with a bandpass filter for 550 ± 20 nm. Each white box represents the integration area used for the intensity calculation. The ring was divided into 24 segments according to the experimental resolution. Fig. S14C shows the histogram of the scattering intensities of these 24 segments. Values for $\sigma_{SCA,ring}$ of the ring were calculated using eq. S1. Table S2 shows the mean scattering intensity and $\sigma_{SCA,ring}$ of the 24 ring segments for wavelengths of 800 ± 20, 700 ± 20, and 550 ± 20 nm.

Table S2: Summary of the mean scattering intensity, $\sigma_{SCA,ring}$, and σ_{SCA} for the 24 ring segments (error is the standard deviation)

Detection window	$I_{SCA,ring}$ (MHz)	$\sigma_{SCA,ring}$ (nm^2)	σ_{SCA} (nm^2)
550 ± 20 nm	7.9 ± 2.0	$(2.2 \pm 0.6) \times 10^4$	560 ± 128
700 ± 20 nm	29.0 ± 8.3	$(2.5 \pm 0.7) \times 10^4$	656 ± 177
800 ± 20 nm	12.8 ± 4.8	$(2.3 \pm 0.8) \times 10^4$	608 ± 247

Fig. S14D displays the $\sigma_{SCA,ringt}$ histogram of the NP ring. The numbers of NPs for each ring segment were also acquired by overlaying Fig. S14B with the SEM image and counting the number of NPs for each white box (Fig. S15A). The normalized σ_{SCA}, which represents $\sigma_{SCA,ring}$ per NP, was calculated by $\sigma_{SCA,ring}/N$ where N is the number of NPs for each ring segment. σ_{SCA} at 800 ± 20, 700 ± 20, and 550 ± 20 nm are also listed in Table S2.
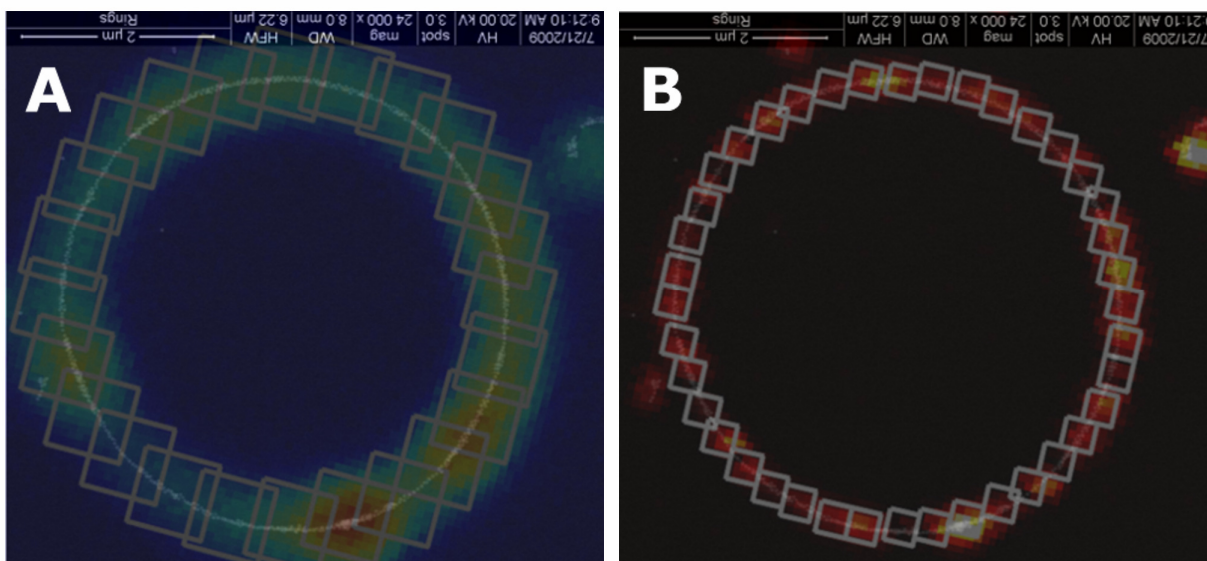
Fig. S15 Scattering (A) and absorption (B) images overlaid with the SEM image allowing the determination of the average number of NPs per integration area.

Calculation of σ_{ABS} for the NP ring

The calculation of σ_{ABS} for the NP ring was similar to that of σ_{SCA}. Photothermal images were acquired from the same NPs analyzed in the scattering experiments using circularly polarized excitation. The excitation wavelengths for the 22 x 70, 33 x 63, and 96 nm NPs were 785, 675, and 514 nm, respectively. The excitation and probe powers ranged between 8 - 54 and 99 -127 kW/cm^2 for the different samples to avoid signal saturation. Fig. S16A shows a photothermal image of 96 nm NPs excited at 514 nm. Each white box corresponds to the area used to calculate the intensity, which was chosen to be 390 x 390 nm^2 based on the optical resolution of the photothermal images. Photothermal images for 22 x70 and 33 x 63 nm NPs were also measured, using 785 and 675 nm excitation. The measured absorption intensities ($I_{ABS,NP}$) of each sample are given in Table S3. The calculated $\sigma_{ABS,NP}$ for these samples at 785, 675, and 514 nm using the simulated spectra in Fig. S13B are also listed in Table S3.

17
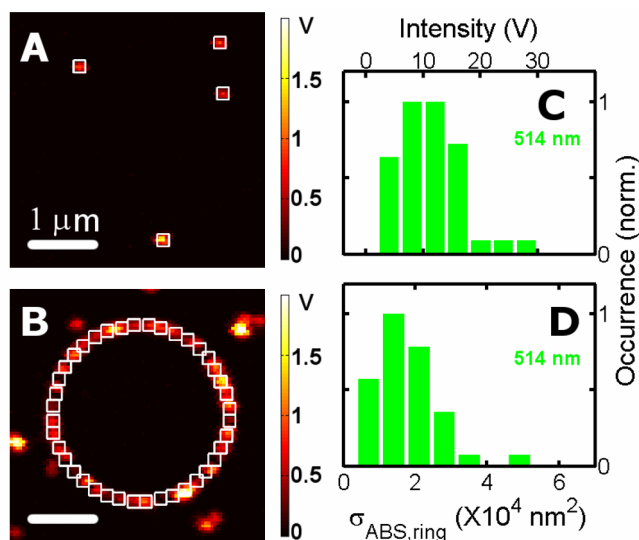
Fig. S16 Calculation of σ_{ABS} for a NP ring. (A), (B) Photothermal images (6.7 x 6.7 µm^2) of 96 nm NPs and the NP ring for 514 nm excitation, respectively. The white boxes (390 x 390 nm^2) present the integration areas used for the intensity calculation. (C) Histogram of integrated absorption intensities for the NP ring, where the integrated area corresponds to the size of the white boxes in (B). (D) Histogram of $\sigma_{ABS,ring}$ for the NP ring calculated using eq. S2.

Table S3: Summary of the absorption intensity and σ_{ABS} for individual NPs (error is standard the deviation)

Sample (excitation wavelength)	$I_{ABS,NP}$ (V)	$\sigma_{ABS.NP}$ (nm^2)
96 nm (514 nm)	9.6 ± 4.8	1.5×10^4
33 x 63 nm (675 nm)	14.1 ± 6.0	4.5×10^3
22 x 70 nm (785 nm)	3.2 ± 1.2	9.6×10^3

The photothermal images of the NP ring were also measured with 785, 675, and 514 nm excitation and circular polarization. The photothermal images of the NP ring and NPs were again measured side-by-side for each wavelength to ensure the same experimental conditions. Fig. S16B shows the photothermal image of the NP ring with 514 nm excitation. The white boxes represent the same integration areas for calculating the experimental absorption intensity as was used for the single NPs (390 x 390 nm^2). The ring was therefore divided into 40 segments. Fig.

S16C displays a histogram of absorption intensities ($I_{ABS,ring}$) for 40 ring segments. Values

for $\sigma_{ABS,ring}$ of the NP ring were calculated using eq. S2.

$$\sigma_{ABS,ring} = \sigma_{ABS,NP} \times \frac{I_{ABS,ring}}{I_{ABS,NP}}$$ (S2)

Table S4 shows the mean absorption intensity and $\sigma_{ABS,ring}$ of the 40 ring segments for 514, 675,

and 514 nm excitation.

Table S4: Summary of the mean absorption intensity, $\sigma_{ABS,ring}$, and σ_{ABS} for the 40 ring segments
(error is the standard deviation)

Excitation wavelength	$I_{ABS,ring}$ (V)	$\sigma_{ABS,ring}$ (nm^2)	σ_{ABS} (nm^2)
514 nm	11.0 ± 5.3	$(1.7 \pm 0.8) \times 10^4$	1205 ± 570
675 nm	13.4 ± 16.8	$(4.3 \pm 5.3) \times 10^3$	335 ± 544
785 nm	4.6 ± 3.4	$(1.4 \pm 1.0) \times 10^4$	988 ± 830

Fig. S16D shows a histogram of $\sigma_{ABS,ring}$ obtained from the 40 ring segments. The

number of NPs within each segment was again acquired by overlaying Fig. S16B with the SEM

image and counting the number of NPs for each white box (Fig. S15B). The normalized σ_{ABS},

which represents $\sigma_{ABS,ring}$ per NP, was calculated by $\sigma_{ABS,ring}/N$ where N is the number of NPs for

each ring segment. The mean values of σ_{ABS} for the 40 rings segments at 785, 675, and 514 nm

are listed in Table S4.

Although the excitation volume contained ~ 15 NPs in the case of the NP ring, the

photothermal signal is dominated by changes in the refractive index of the medium and not the

NPs themselves as shown by photothermal imaging of single NPs in different media(3),

justifying the analysis chosen here. In addition, the good agreement between the measured

photothermal intensities and calculated values for various NP sizes further verifies the accuracy

of photothermal imaging in determining SP absorption regardless of the volume of the NPs

probed in the excitation area(4).
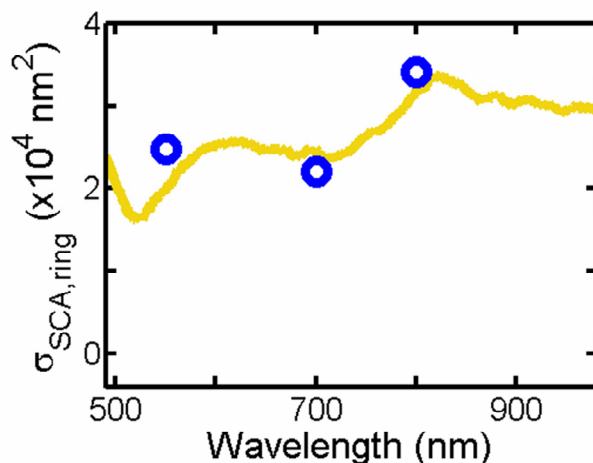
Fig. S17 $\sigma_{SCA,ring}$ (blue) at 550, 700 and 800 nm of the ring segment marked by the yellow rectangle in Fig. 1A. The yellow line shows the scattering spectrum of the same ring segment.

References

1. Wilbur JL, Kumar A, Biebuyck HA, Kim E, Whitesides GM (1996) Microcontact printing of self-assembled monolayers: applications in microfabrication *Nanotechnology* 7: 452.

2. Berciaud S, Cognet L, Blab GA, Lounis B (2004) Photothermal heterodyne imaging of individual nonfluorescent nanoclusters and nanocrystals *Phys Rev Lett* 93: 257402/1-4.

3. Gaiduk A, Ruijgrok PV, Yorulmaz M, Orrit M (2010) Detection limits in photothermal microscopy *Chem Sci* 1: 343-350.

4. Tcherniak A, Ha JW, Dominguez-Medina S, Slaughter LS, Link S (2010) Probing a Century Old Prediction One Plasmonic Particle at a Time *Nano Lett* 10: 1398-1404.